Journal of Materials Chemistry A



PAPER

View Article Online
View Journal | View Issue



Cite this: J. Mater. Chem. A, 2017, 5, 18012

Organic-inorganic hybrid electrolytes from ionic liquid-functionalized octasilsesquioxane for lithium metal batteries†

Guang Yang, (D) Chalathorn Chanthad, Hyukkeun Oh, Ismail Alperen Ayhan and Qing Wang (D)*

The use of highly conductive solid-state electrolytes to replace conventional liquid organic electrolytes enables radical improvements in the reliability, safety and performance of lithium batteries. Here, we report the synthesis and characterization of a new class of nonflammable solid electrolytes based on the grafting of ionic liquids onto octa-silsesquioxane. The electrolyte exhibits outstanding room-temperature ionic conductivity (\sim 4.8 \times 10⁻⁴ S cm⁻¹), excellent electrochemical stability (up to 5 V relative to Li⁺/Li) and high thermal stability. All-solid-state Li metal batteries using the prepared electrolyte membrane are successfully cycled with high coulombic efficiencies at ambient temperature. The good cycling stability of the electrolyte against lithium has been demonstrated. This work provides a new platform for the development of solid polymer electrolytes for application in room-temperature lithium batteries.

Received 26th May 2017 Accepted 28th July 2017

DOI: 10.1039/c7ta04599a

rsc.li/materials-a

Introduction

Lithium ion batteries are widely used in portable electronics and hybrid electric vehicles due to their high energy density, high efficiency and long life.1-4 One of the major efforts in the development of next-generation lithium batteries to meet the future challenges of transportation and clean energy storage has focused on the synthesis and characterization of polymer electrolytes.4-7 Current rechargeable lithium batteries to power portable electronic devices and electric vehicles use a flammable mixture of carbonate solvents in electrolytes, which create safety and reliability concerns.^{2,8} Furthermore, the presence of liquid electrolytes prevents the utilization of highly energetic metallic lithium anodes owing to the reactivity of the highly volatile organic solvents and the formation of lithium dendrites that may give rise to thermal runaway and even explosions. It is thus expected that the replacement of the conventional liquid organic electrolytes by solid-state electrolytes significantly improves the safety characteristics of highenergy batteries. For the application of solid-state electrolytes in batteries, they have to concurrently possess a range of desirable properties such as high thermal stability, good mechanical strength, and a wide electrochemical stability window in addition to high ionic conductivity.2,3,5,9-11

Department of Materials Science and Engineering, The Pennsylvania State University, University Park, Pennsylvania 16802, USA. E-mail: wang@matse.pu.edu

To date, poly(ethylene oxide) (PEO), a semicrystalline polymer, complexed with lithium salts such as lithium bis(trifluoromethylsulfonyl)imide (LiTFSI) has been the most widely studied and best polymer electrolyte. However, PEO exhibits poor conductivities ($i.e. \sim 10^{-6} \, \mathrm{S \ cm^{-1}}$) at room temperature as a result of crystallization. A practically useful conductivity value ($\geq 10^{-4} \, \mathrm{S \ cm^{-1}}$) can only be achieved in PEO based polymer electrolytes above 70 °C which corresponds to the semicrystalline–amorphous phase transition temperature of PEO. The addition of organic solvents that are able to compete with the polymer ether oxygens for Li⁺ cation coordination has been demonstrated as a means of attaining a high ionic conductivity at room temperature. Of these solvents still poses safety concerns.

More recently, much attention has been devoted to the investigation of alternative solid electrolytes to the state-of-the-art. In particular, ionic liquids (ILs) offer many attractive features as electrolytes, including non-flammability, excellent chemical and electrochemical stability, negligible vapor pressure and high ionic conductivity. Solidification of ILs including polymerization of IL-containing monomers and grafting ILs onto inorganic nanoparticles has thus been carried out and the resulting materials have been explored as solid-state electrolytes for lithium batteries. However, the immobilized ILs have not shown much improved ionic conductivity in comparison to PEO based polymer electrolytes, e.g. 10^{-5} S cm⁻¹ at room temperature, although the plasticized solid electrolytes containing additives such as organic solvents and ILs show much improved conductivity values. Sec. 26.27

[†] Electronic supplementary information (ESI) available: NMR, DSC, TGA, XRD, EIS, stripping/plating tests, Raman, and battery performance. See DOI: 10.1039/c7ta04599a

Herein, we report the preparation and characterization of a novel class of solid electrolytes based on ionic liquidfunctionalized polyhedral oligomeric silsesquioxanes (POSS-IL). The electrolyte not only is nonflammable but also exhibits an impressive ionic conductivity of 4.8 \times 10⁻⁴ S cm⁻¹ at 25 $^{\circ}$ C when doped with LiTFSI and a large electrochemical stability window approaching 5 V. We further demonstrate the successful operation of Li/Li₄Ti₅O₁₂ (LTO) and Li/LiFePO₄ (LFP) batteries at 25 °C using the prepared solid electrolyte. This is especially noticeable because the state-of-the-art all-solid-state polymer electrolytes are typically cycled at elevated temperatures. 15,28,29

Experimental

Materials

Octasilane polyhedral oligomeric silsesquioxane (POSS) was purchased from Hybrid Plastics and dried at 60 °C under vacuum overnight before use. Hexaethylene glycol (97%), triphenyl phosphine (99%), tetrabromomethane (CBr₄, 99%), trichlorovinylsilane (97%), lithium bis(trifluoromethanesulfonyl) imide (LiTFSI), Karstedt catalyst solution in xylene (2%), 1-butyl imidazole (98%), anhydrous acetonitrile, anhydrous dimethylformamide (DMF), anhydrous tetrahydrofuran (THF), and anhydrous benzene were purchased from Sigma-Aldrich. Dichloromethane, diethyl ether, ethyl acetate, chloroform, and methanol were purchased from VWR.

Synthesis of 17-bromo-3,6,9,12,15-pentaoxaheptadecan-1-ol

In a 50 mL flask equipped with a magnetic stirrer, hexaethylene glycol (hEG, 10 g, 35.42 mmol) and triphenyl phosphine (4.65 g, 17.71 mmol) were dissolved in 25 mL anhydrous THF at 30 °C. The reactor was purged with nitrogen for 35 min before CBr₄ (5.87 g, 17.71 mmol) was added. The reaction was allowed to proceed for 4 hours at 30 °C under a nitrogen atmosphere. The solution was then concentrated on a rotary evaporator at 50 °C and the crude product was purified by column chromatography with chloroform/methanol (95:5 v/v) to give 17-bromo-3,6,9,12,15-pentaoxaheptadecan-1-ol as slight yellow oil (81%). ¹H NMR (300 MHz, CDCl₃, ppm) δ : 3.02 (s, -OH), 3.48 (t, -CH₂-Br), 3.59-3.73 (m, $-O-C\underline{H}_2-$), 3.79 (t, $-C\underline{H}_2-CH_2-Br$); ^{13}C NMR (CDCl₃, ppm) δ: 30.1, 61.6, 70.2–70.7 (br), 73.0 (-CH₂-CH₂-Br).

Synthesis of vinyl tris-17-bromo-3,6,9,12,15pentaoxaheptadecan-1-ol silane (3)

In a 100 mL flask equipped with a magnetic stirrer, 17-bromo-3,6,9,12,15-pentaoxaheptadecan-1-ol (5.6 g, 0.016 mol) and triethylamine (3.2 g, 0.032 mol) were dissolved in toluene (50 mL) at room temperature. The reactor was purged with nitrogen for 40 min before trichlorovinylsilane (0.873 g, 5.33 mmol) was added dropwise. The reaction mixture was stirred for 3 hours at room temperature under a nitrogen atmosphere. The product solution was then diluted with ethyl acetate (50 mL), washed with de-ionized water and dried over anhydrous Na₂SO₄. The organic layer was separated, concentrated, and dried under vacuum at 60 °C to give product 3 (84%). ¹H NMR (300 MHz, $CDCl_3$, ppm) δ : 3.43 (t, $-C\underline{H}_2$ -Br), 3.58-3.68 (m, $-O-C\underline{H}_2$ -), 3.79 ($-O-C\underline{H}_2$ -) CH_2-CH_2-Br), 3.89 (t, $-Si-O-CH_2-$), 5.9-6.1 (m, $CH_2=CH-Si-$); ¹³C NMR (CDCl₃, ppm) δ : 30.1, 62.4 (-Si-O-CH₂), 70.8-71.9 (signal overlap), 72.7 ($\underline{C}H_2$ - $\underline{C}H_2$ - $\underline{B}r$), 137.4 ($\underline{C}H_2$ = $\underline{C}H$ - $\underline{S}i$ -).

Synthesis of POSS-IL

In a 50 mL flame dried flask equipped with a magnetic stirrer, POSS (640 mg, 0.63 mmol) and compound 3 (5.48 g, 5.04 mmol) were dissolved in anhydrous benzene (20 mL) at room temperature. The reactor was degassed by bubbling with nitrogen for 1 h. 2 drops (14 µL) of the Karstedt catalyst were added subsequently. The mixture was stirred in an oil bath at 50 °C for 48 h. Then the solvent was evaporated on a rotary evaporator and dried in a vacuum at 60 °C to give compound 4. Then 4 was dissolved in DMF (20 mL) and 1-butyl imidazole (2.04 g, 16.43 mmol) was added. The solution was stirred at 40 °C under N2 for 24 h. After the removal of the solvent, the product was mixed with LiTFSI (4.72 g, 16.43 mmol) in anhydrous acetonitrile (20 mL). The mixture was stirred for 24 h at room temperature before the solvent was evaporated. The product was redissolved in dichloromethane and lithium bromide was removed by filtration. The final products were purified by washing with diethyl ether several times, and then the product was dried under vacuum to give final product 6: POSS-IL: ¹H NMR (300 MHz, DMSO-d₆, ppm) δ : 0.90 (t, -C<u>H</u>₃), 1.26 (m, -CH₂-CH₂-CH₃), 1.78 (m, -CH₂-CH₂-CH₃), 3.42-3.60 $(m, -O-CH_2-), 4.20 (t, O-CH_2-CH_2-N-), 4.35 (t, -N-CH_2-CH_2-),$ 7.78 (d, -N-CH=CH-N-), 9.18 (s, -N=CH-N-).

Characterization

The chemical structures of the polymers were determined by ¹H and ¹³C NMR on a Bruker AM-300 Nuclear Magnetic Resonance Spectrometer. FTIR spectra were obtained using a Bruker Vertex 70 spectrometer. Raman spectra were measured on a Horiba LabRam HR Evolution equipped with an Oxxius DPSS 532 nm laser and a Horiba Synapse EM detector. Analysis of the peak around 742 cm $^{-1}$ was performed with the 1800 g mm $^{-1}$ grating which yields a spectral resolution of 0.4 cm⁻¹. We tested for laser beam damage and found that all species measured with Raman were stable even at the maximum incident power of 45 mW. All thermal analysis Raman measurements presented in this paper were performed with an acquisition time of 30 s, a 50 µm confocal pinhole and 2 accumulation to account for any interference. A Linkam HFS600 temperature stage was used to change the environmental temperature and the objective used was an Olympus 50× LMPLFLN with a numerical aperture of 0.5. At each temperature set point there was a wait time of >10 min before each measurement to ensure that the temperature of the sample had stabilized. Pulse field gradient NMR (PFG-NMR) diffusion measurements were performed using a Bruker Avance-III-HD-500 MHz, 11.7 T, prodigy probe. Spectrometer frequencies for ⁷Li and ¹⁹F are 194.4 MHz and 470.6 MHz. Signal attenuation parameters: the diffusion delay (Δ) ranges from 0.1–0.6 s, the gradient pulse length (δ) is 6 ms, the gradient pulse

magnitude (g) ranges from 0–50 G cm⁻¹, and the relaxation delay is 10 s.

X-ray photoelectron spectroscopy (XPS) experiments were performed using a Physical Electronics VersaProbe II instrument equipped with a monochromatic Al ka X-ray source $(h\nu = 1486.7 \text{ eV})$ and a concentric hemispherical analyzer. Charge neutralization was performed using both low energy electrons (<5 eV) and argon ions. The binding energy axis was calibrated using sputter cleaned Cu foil (Cu 2p_{3/2} = 932.7 eV and Cu $2p_{3/2} = 75.1$ eV). Peaks were charge referenced to the CH_x band in the carbon 1 s spectra at 284.8 eV. Measurements were made at a takeoff angle of 45° with respect to the sample surface plane. This resulted in a typical sampling depth of 3-6 nm (95% of the signal originated from this depth or shallower). Quantification was done using instrumental relative sensitivity factors (RSFs) that account for the X-ray cross-section and inelastic mean free path of the electrons. The curves were fitted using a mixed Gaussian/Lorentzian profile.

The glass transition temperature (T_g) was measured on a TA Q100 differential scanning calorimeter (DSC) at a heating and cooling rate of 10 °C min⁻¹ in the temperature range from -80 to 100 °C. Thermogravimetric analysis (TGA) measurements were performed on a TA Instrument model Q50 at a heating rate of 10 °C min⁻¹ under N₂ from room temperature up to a maximum of 800 °C to study the thermal stability. Wide-angle X-ray diffraction (WAXD) was performed on a Rigaku DMAX-Rapid Microdiffractometer equipped with a 2-D detector, also using CuK_{α} radiation. The software routines were used to evaluate the scattering intensity as a function of the diffraction angle of 2θ , or q, defined as $q = 4\pi \sin(\theta)/\lambda$.

Dynamic shear moduli were measured using an RDS-IIE rheometer. The POSS-IL sample was placed between two parallel plates with a diameter of 25 mm. The shear strain was varied to obtain the storage modulus (G') and loss modulus (G'') at room temperature.

The ionic conductivity (σ) was measured by Broadband Dielectric Relaxation Spectroscopy (DRS). Measurements were performed on a Concept 40 system from Novocontrol GmbH over the frequency range of 10 mHz to 10 MHz. The temperature was controlled using a Quatro temperature control system with a precision of greater than ± 0.1 °C. All polymers were measured over the temperature range from -25 °C to 80 °C. To prepare samples for DRS measurements, the polymer electrolyte solutions were cast onto stainless steel electrodes and dried under vacuum overnight at 60 °C.

Electrochemical impedance spectroscopy (EIS) was used to study the interfacial properties of Li/Li symmetrical cells using a PAR 2273 FRA/potentiostat. The lithium transference number (t_{Li^+}) of the electrolyte was also calculated from the results obtained from the Nyquist plots measured by EIS (1 MHz to 100 mHz, 20 mV AC voltage). t_{Li^+} was calculated according to the method reported by Bruce and Vincent³⁰ (a combination of AC impedance and DC polarization measurements) which was widely used for the determination of t_{Li^+} of the polymer-IL-Li salt system. The equation can be written as $t_{\text{Li}^+} = I_s(V - I_iR_i)/I_i(V - I_sR_s)$, where V is the constant DC voltage applied; I_i and I_s are the initial and steady state current, and R_i and R_s are the

interfacial resistance before and after DC polarization. A DC voltage of 30 mV was applied to the two lithium electrodes. Voltammetry experiments were performed on a PAR Potentiostat/ Galvanostat Model 263A using a sealed cell with synthesized polymer electrolytes sandwiched between a stainless steel disk working electrode and a lithium foil counter/reference electrode aided by a Teflon o-ring spacer with an inner diameter of 1 cm. Tests were done at a scan rate of 1 mV s $^{-1}$ at 25 $^{\circ}$ C.

Cell assembly and battery performance. The synthesized polymer electrolyte was dissolved in anhydrous THF (11% w/v) in a glove box. LiTFSI was then added to the above solution. Coin cells (CR2032) were assembled in an argon-filled glove box (Labstar MB10, MBRAUN). Li₄Ti₅O₁₂ (LTO, Ishihara Sangyo Kaisha, Ltd.) and LiFePO₄ (LFP, Sud-Chemie) were selected as cathode materials (slurries containing 80 wt% of LTO or LFP, 10 wt% of super P (a carbon additive to enhance electrode conductivity) and 10 wt% of POSS-IL in 1-methyl-2-pyrrolidone (NMP) were made and cast onto 9 µm thick copper foil (15 µm thick aluminum foil was used for LFP) followed by the doctor blade method). The areal density of the active material was ca. 2.8 mg cm⁻². The cathode sheets were punched into 1 cm diameter (0.785 cm²) disks, vacuum dried at 80 °C completely, weighed, and transferred into a glove box for coin cell assembly. Lithium foils (MTI, 250 µm thick) were used as the anode. The polymer electrolyte solution was cast on the anode and the solvent was evaporated in a glove box leaving the solvent-free polymer electrolyte membrane. The coin cell was assembled by sandwiching the solvent-free polymer electrolyte between the cathode and anode in the coin cell case with a 125 µm ring shaped Teflon spacer. Battery tests were performed on a Neware CT-3008 battery tester. The theoretical capacities of LTO and LFP were 175 mA h g^{-1} and 170 mA h g^{-1} , respectively.³⁴ An ESPEC BTU-133 temperature chamber was used to change the environmental temperature for the coin cells. The batteries were cycled between 1.3 to 2.0 V for the Li/POSS-IL-LiTFSI/LTO cell and 2.5 to 3.9 V for the Li/POSS-IL-LiTFSI/LFP cell under constant current conditions. A conventional liquid electrolyte (1 M LiTFSI in ethylene carbonate-dimethyl carbonate (EC-DMC, 1:1, v/v)) was used as a control in the lithium stripping/plating and galvanostatic polarization tests.

Field emission scanning electron microscopy (FEI NanoSEM 630 FESEM) was used to study the electrode surface morphology.

The flammability test was performed with a Master Microtorch fed with butane flux; inert glass fiber filter strips with 1 cm width and 0.6 μ m pore size were soaked in the concentrated POSS-IL solution in anhydrous THF for 5 min. Then these strips were dried and placed at a fixed distance from the microtorch before testing. As a control, the glass fiber filter was also soaked in the liquid electrolyte (1 M LiTFSI EC-DMC, 1:1, v/v).

Results and discussion

As shown in Scheme 1, the synthesis of POSS-IL involves the hydrosilylation of octakis(dimethyl-siloxy)silsesquioxane with vinyl *tris*-17-bromo-3,6,9,12,15-pentaoxaheptadecan-1-ol silane (3) followed by quaternization using 1-butyl imidazole.

Scheme 1 Synthesis of POSS-IL

The ¹H NMR spectra of intermediates are shown in Fig. S1-S3.† In Fig. 1, the disappearance of the peaks at 5.9-6.0 ppm attributed to the vinyl group and Si-H protons at 5.1 ppm in the ¹H spectrum of POSS-IL confirms the completion of the hydrosilylation reaction. This is also supported by the absence of the Si-H stretching peak at 2140 cm⁻¹, the Si-H bending peak at 900 cm⁻¹, and the -CH₂=CH- stretching peak at 1640 cm⁻¹ in the FTIR spectrum of POSS-IL (Fig. 2 left). The tethered IL ion pairs in POSS-IL have been characterized by X-ray photoelectron spectroscopy (XPS), in which two major peaks at 401.7 and 399.1 eV are assigned to N atoms in the imidazolium ring (N⁺) and TFSI⁻ anion (N⁻) respectively.³⁵ The peak intensity ratio of N^+/N^- was found to be $\sim 2.1:1$, validating the expected 1:1 ratio of the cation and anion in POSS-IL (Fig. 2 right).

The glass transition temperature (T_g) of POSS-IL was determined to be -33 °C by DSC, which increases to -31 °C upon doping with LiTFSI (Fig. S5†). TGA reveals that POSS-IL is thermally stable up to ~ 250 °C (Fig. S6†). The absence of the melting transition in the DSC thermogram of POSS-IL suggests its amorphous nature, which has been further corroborated in the presence of broad diffraction peaks in WAXD patterns (Fig. S7†). Fig. 3 shows the strain-dependent dynamic moduli of POSS-IL measured in an oscillatory shear flow as a function of applied strain amplitude with a fixed frequency ($\omega = 10 \text{ rad s}^{-1}$).

The individual elements interact strongly with other molecules nearby (so-called "neighbours") to yield "cage"-like aggregates.

At low shear strain (i.e. <10%), the storage modulus (G') is greater than the loss modulus (G"), a characteristic of solidelastic materials. With the increase of shear strain, a gradual

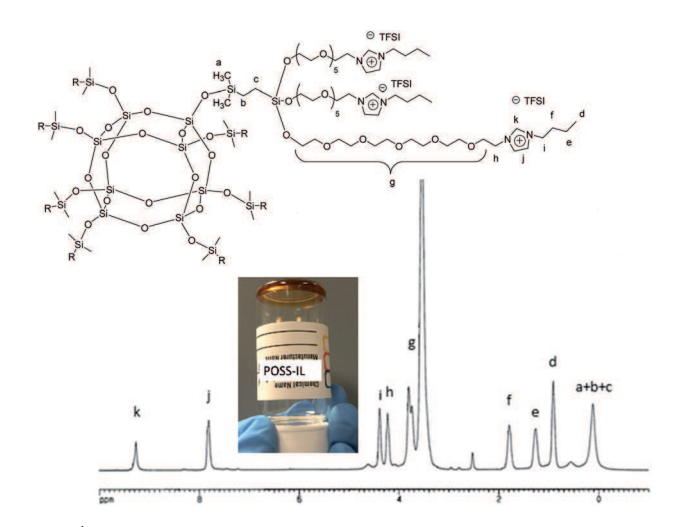


Fig. 1 ¹H NMR spectrum of POSS-IL.

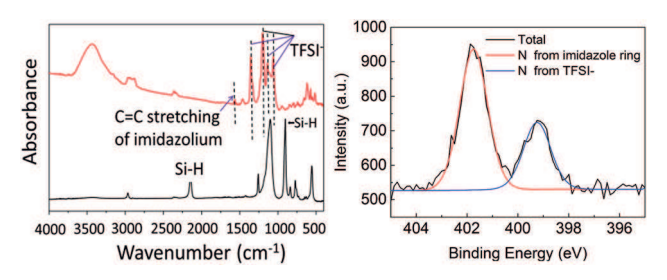


Fig. 2 (Left) FTIR spectra of POSS (black) and POSS-IL (red). (Right) X-ray photoelectron spectroscopy N 1s spectrum of POSS-IL.

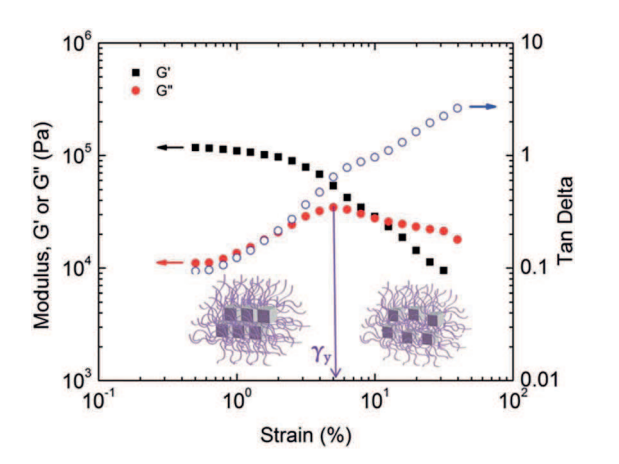


Fig. 3 The dynamic shear moduli (G', G'') and tan delta of POSS-IL as a function of applied strain at 25 °C.

decrease in G' and the concomitant appearance of a maximum in G'' are indicative of the soft glassy nature of POSS-IL. ^{36,37} Soft glassy materials are individual elements trapped in tight cages produced by interaction with their neighbors as shown in the left image of Fig. 3. POSS-IL exhibits solid features before critical strain γ_y where the cages break. Solution-cast films of POSS-IL can be successfully prepared owing to the entanglement of

the long chains grafted onto POSS. The non-flammability of POSS-IL has been verified in the ignition tests as shown in Fig. $S14.\dagger$

The temperature dependence of the ionic conductivity (σ) of POSS-IL doped with LiTFSI ([EO]:[Li] = 12:1), measured by broadband dielectric relaxation spectroscopy, is presented in Fig. 4. The POSS grafted with PEO side chains (POSS-PEO, shown in Fig. S4†) has been prepared and characterized for the purpose of comparison. Clearly, the σ of POSS-IL is much greater than that of POSS-PEO over the temperature range of -25 to 80 °C. At 25 °C, the σ of POSS-IL/LiTFSI reaches $4.8 \times 10^{-4} \text{ S cm}^{-1}$, which, to the best of our knowledge, is among the highest room-temperature conductivities reported so far for solvent-free organic/polymeric material-based solid Li⁺ electrolytes. 20,38-41 On the other hand, POSS-PEO/LiTFSI exhibits a σ of 5.6 \times 10⁻⁶ S cm⁻¹ at 25 °C, which is almost two orders of magnitude lower than that of POSS-IL. The σ value of POSS-PEO is consistent with the literature results on PEObased solid electrolytes measured at room temperature.29,42 Such a large difference in ionic mobility between POSS-IL and POSS-PEO is attributed to the presence of imidazolium rings at the chain ends in POSS-IL, in which the positively charged imidazole would interact with TFSI- anions by electrostatic force to facilitate the liberation of Li⁺ from LiTFSI salts for higher mobility. To verify this hypothesis, Raman spectroscopy was employed to study the conformations of TFSI anions in the samples because the expansion-contraction mode of TFSI⁻ anions at ~742 cm⁻¹ in Raman spectra is sensitive to their conformational changes. As shown in Fig. 5, the Raman peak at 742 cm⁻¹ can be fitted into three conformers using Gaussian/ Lorentzian functions: C_1 , C_2 , and C_{coord} . C_1 (cisoid) and C_2 (transoid) conformers stem from free TFSI⁻ anions and C_{coord} originates from Li⁺ coordinated TFSI⁻ anions. 43,44 It is found that the relative peak intensity of $C_{\rm coord}$ in POSS-IL is much weaker than that of C_{coord} in POSS-PEO, indicative of much more uncoordinated, free Li+ ions existing in POSS-IL. In addition, as shown in Fig. S8† where the POSS-PEO-LiTFSI Raman spectrum is subtracted from the POSS-IL-LiTFSI spectrum, the appearance of the positive peak at around 740 cm⁻¹ represents more free TFSI⁻ anions in POSS-IL-LiTFSI, whereas the negative peak at 746 cm⁻¹ stands for less Li⁺ coordinated TFSI anions in POSS-IL-LiTFSI.

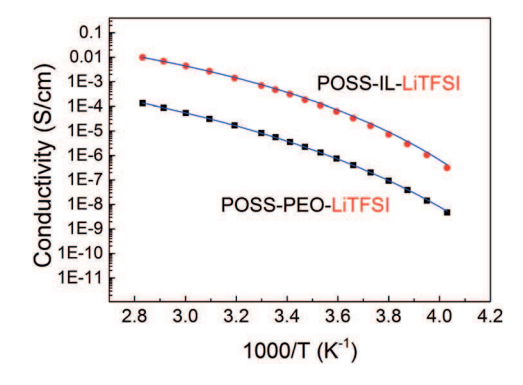


Fig. 4 Temperature dependence of the ionic conductivity of POSS-IL-LiTFSI and POSS-PEO-LiTFSI ([EO]:[Li] = 12:1).

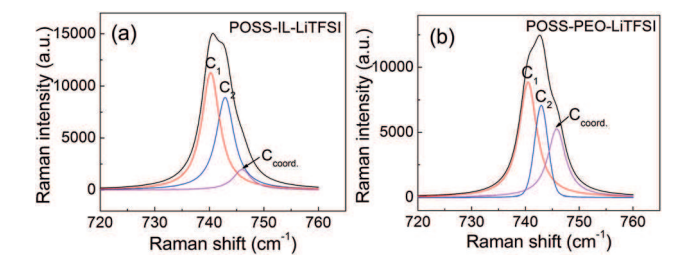


Fig. 5 Raman spectra for TFSI⁻ anion vibration of (a) POSS-IL-LiTFSI and (b) POSS-PEO-LiTFSI at 25 °C in the range of 720-760 cm⁻¹.

Table 1 Ionic conductivity values at room temperature and fitting parameters

	σ (25 °C, S cm ⁻¹)	<i>r</i> -Square	B (kJ mol ⁻¹)	$A (S cm^{-1} K^{1/2})$
POSS-IL-LiTFSI		0.999	9.2	125.8
POSS-PEO-LiTFSI		0.999	12.2	7.7

The temperature dependence of the σ of POSS-IL shows empirical Vogel-Tammann-Fulcher (VTF) behavior, suggesting that ion conduction is related to molecular relaxation and swinging motions of chains tethered to POSS. For the VTF equation, $\sigma = AT^{-1/2} \exp(-B/R(T-T_0))$, where A is a constant proportional to the number of charge carriers, B is equivalent to the activation energy for ion motion, R is the gas constant, T is the experimental temperature, and T_0 is an empirical reference temperature. The calculated VTF parameters A, B and T_0 for POSS-IL are provided in Table 1, and the fitting curves are plotted in Fig. 4 as solid lines. A lower activation energy is found in POSS-IL in comparison to POSS-PEO, i.e. 9.2 vs. 12.2 kJ mol⁻¹, signifying a lower energy barrier in POSS-IL for Li⁺ conduction.

The interfacial stability of POSS-IL against the lithium electrode was characterized by EIS. From the Nyquist plot of symmetrical Li/ electrolyte/Li cells as a function of storage time (Fig. S9a†), the intercept at the real axis at the high frequency part represents bulk electrolyte resistance (R_b) and the length between the intercepts of the semicircle at the real axis denotes interfacial resistance (R_{int}) . The data points were fitted by using Z-view software and the equivalent circuit is shown in the inset of Fig. S9a, \dagger in which R_1 is the bulk resistance, R_2 is the interfacial resistance, and CPE and W

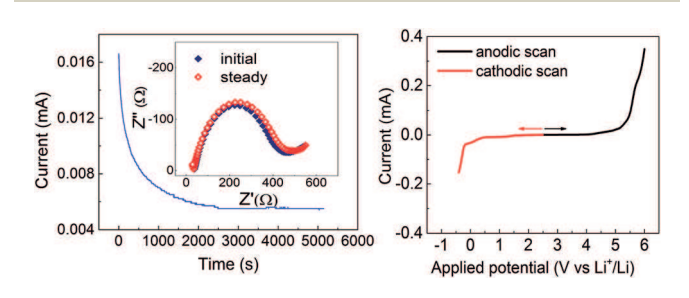


Fig. 6 (Left) chronoamperometry profile of the Li/POSS-IL-LiTFSI/Li cell and the inset shows Nyquist plots at 25 °C. (Right) linear sweep voltammetry of POSS-IL-LiTFSI at 25 °C.

stand for the constant phase element and Warburg resistance respectively. As shown in Fig. S9b,† no significant change has been found in R_1 during the time frame, revealing the good chemical stability of POSS-IL. R2 increases rapidly, which probably results from the reaction between POSS-IL and the lithium electrode to form a passive solid electrolyte interphase (SEI),41 and then stabilizes after 3 days. The ${\rm Li}^+$ transference number $t_{{\rm Li}^+}$ for the POSS-IL electrolyte, measured using the Li/electrolyte/Li configuration according to the steady state current method (Fig. 6 left), is around 0.3, a typical value of PEO based solid-state electrolytes.13 This value of t_{Li^+} is on the high end for PEO/LiTFSI systems, which is ascribed to a high number of free Li⁺ ions as a result of interactions between imidazolium and TFSI-. Moreover, it is thought that the POSS moieties in the hybrid structures may absorb TFSI- and reduce TFSI⁻ mobility, which also contributes to the improved t_{Li^+} value. 45 We have also performed PFG-NMR diffusion measurements on POSS-IL-LiTFSI. The self-diffusion coefficients obtained are Li⁺ ($D_{\rm Li} = 6.9 \times 10^{-12} \ {\rm m}^2 \ {\rm s}^{-1}$) and TFSI⁻ ($D_{\rm TFSI}=1.2\times10^{-11}~{
m m}^2~{
m s}^{-1}$). The $t_{
m Li^+}$ calculated from $D_{
m Li}/(D_{
m Li}$ + D_{TESI}) is 0.36.

As shown in the linear sweep voltammogram (Fig. 6 right), the major anodic decomposition potential was found at around 5 V vs. Li⁺/Li. On the cathodic side, a very slight and broad reduction profile was observed in the 0.3-1.4 V range, indicating a stable SEI film preventing further electrolyte reduction. 46,47 To study the lithium deposition stability in the presence of POSS-IL, galvanostatic cycling (stripping/plating) tests were carried out on the Li/Li symmetrical cell, in which a constant current of 0.05 mA cm^{-2} was applied on the cell and reversed every hour. From the plot shown in the left figure of Fig. S11,† the overpotential value increases at the initial period, indicating the increase of internal resistance that may be related to the thickening of the SEI layer, and then remains stable after 440 h. No short circuit was observed after 600 h. In stark contrast, the cells using the liquid electrolyte (1 M LiTFSI in EC-DMC) exhibit unstable overpotential profiles (Fig. S11† right). The results proved the excellent cycling stability of POSS-IL against lithium. Fig. 7 shows the surface morphology of the lithium foils disassembled from button cells after the stripping/plating tests. It can be seen that the lithium electrode surface using POSS-IL as the electrolyte after 440 h cycling has sporadic lithium deposits and is much smoother than the lithium surface using the liquid

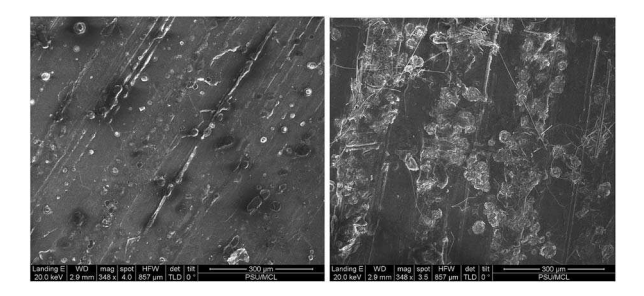


Fig. 7 The surface morphology of the lithium foil after the stripping/ plating test characterized by SEM. (Left) POSS-IL group after 440 h cycling. (Right) 1 M LiTFSI in ED/DMC (1:1, v/v) group after 40 h cycling (scale bar, 300 µm).

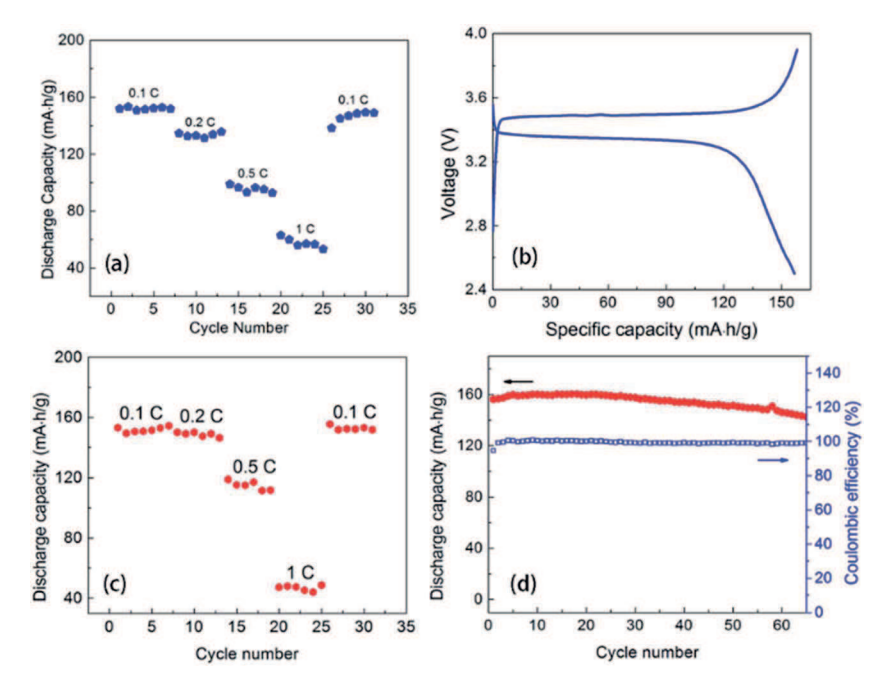


Fig. 8 (a) Rate performance of the Li/POSS-IL-LiTFSI/Li₄Ti5O₁₂ cell. (b) –(d) are Li/POSS-IL-LiTFSI/LiFePO₄ cell performances. (b) Charge and discharge voltage profiles at 0.1 C. (c) Rate capability test. (d) Cycling stability at 0.1 C. All tests were done at 25 $^{\circ}$ C.

electrolyte after 40 h cycling which presents clear and large dendrites indicating uneven lithium deposition.

All-solid-sate Li/LTO coin cells with POSS-IL/LiTFSI as the electrolyte were assembled to further evaluate the viability of POSS-IL for lithium metal batteries. At 25 °C, from the rate performance result shown in Fig. 8a, the steady decrease of discharge capacity with rates, *e.g.* from 153.6 mA h g $^{-1}$ at 0.1 C to 99.1 mA h g $^{-1}$ at 0.5 C and 62.4 mA h g $^{-1}$ at 1 C, is attributable to the polarization effect and increased interfacial resistance at high rates which decelerates Li $^{+}$ diffusion. 7 A typical charge–discharge profile is shown in Fig. S12a. † The discharge capacity is 154.5 mA h g $^{-1}$ with the retention of 96.8% after 70 cycles (Fig. S12b †).

POSS-IL has been assembled as the electrolyte with the LFP electrode for the coin cells as well. In Fig. 8b, the Li/POSS-IL-LiTFSI/LFP cells display clear charge/discharge potential plateaus near 3.45 V (νs . Li $^+$ /Li) commonly observed for Li/LFP batteries. The coulombic efficiency is around 99% measured at room temperature. The room-temperature rate performance data (Fig. 8c) show that the discharge capacity at 0.2 C is close to the value at 0.1 C, *i.e.* 151 mA h g $^{-1}$, and decreases to 115 mA h g $^{-1}$ at 0.5 C. Comparatively, only 22% of the discharge capacity is retained after 50 cycles for Li/POSS-PEO-LiTFSI/LFP cells operating at 60 °C (Fig. S13†).

The discharge capacity and coulombic efficiency evolution with cycle number is plotted in Fig. 8d. At the initial stage, the specific capacity improved probably due to the enhancement of contact between the electrolyte and electrode. The specific capacity stabilized for about twenty-five cycles before gradually showing a sign of decrease. This is possibly due to electrode material loss, SEI growth, or other side reactions. Although the values of discharge capacity reported herein are comparable to those of most solid-state Li/LFP polymer batteries in the

literature, our batteries are cycled at room temperature, whereas the capacities in other studies are normally obtained at temperatures higher than 70 $^{\circ}$ C. $^{29,51-54}$ Note that there have been only very few reports on all-solid-state polymer electrolytes that successfully support the cycling of lithium secondary batteries at ambient temperature. $^{20,23,38-40,55}$

Conclusion

In summary, we have presented a unique class of organic-inorganic hybrid electrolytes based on IL-grafted POSS. The electrolyte exhibits many remarkable features, including non-flammability, superior room temperature ion conductivity and excellent electrochemical stability, for Li-metal batteries. Prototype batteries using this electrolyte have been successfully cycled at room temperature. The plating–stripping experiments on a symmetrical cell with Li-metal electrodes confirmed the ability of POSS-IL to successfully mediate lithium deposition and dissolution. While considerable work remains to be done, we believe that this work provides a promising structural platform for the development of new solid-state electrolytes for ambient-temperature lithium batteries.

Acknowledgements

This work was supported by the National Science Foundation.

Notes and references

- 1 V. Etacheri, R. Marom, R. Elazari, G. Salitra and D. Aurbach, *Energy Environ. Sci.*, 2011, 4, 3243–3262.
- 2 J. Kalhoff, G. G. Eshetu, D. Bresser and S. Passerini, *ChemSusChem*, 2015, **8**, 2154–2175.

- 3 J. B. Goodenough and K.-S. Park, *J. Am. Chem. Soc.*, 2013, **135**, 1167–1176.
- 4 B. Scrosati and J. Garche, *J. Power Sources*, 2010, **195**, 2419–2430.
- 5 W. H. Meyer, Adv. Mater., 1998, 10, 439-448.
- 6 A. M. Stephan and K. Nahm, Polymer, 2006, 47, 5952-5964.
- 7 E. Quartarone and P. Mustarelli, *Chem. Soc. Rev.*, 2011, **40**, 2525–2540.
- 8 K. Xu, Chem. Rev., 2014, 114, 11503-11618.
- 9 I. Osada, H. de Vries, B. Scrosati and S. Passerini, *Angew. Chem., Int. Ed.*, 2016, 55, 500–513.
- 10 K. K. Fu, Y. Gong, J. Dai, A. Gong, X. Han, Y. Yao, C. Wang, Y. Wang, Y. Chen and C. Yan, *Proc. Natl. Acad. Sci. U. S. A.*, 2016, 113, 7094–7099.
- 11 R. Khurana, J. L. Schaefer, L. A. Archer and G. W. Coates, *J. Am. Chem. Soc.*, 2014, **136**, 7395–7402.
- 12 D. Devaux, R. Bouchet, D. Glé and R. Denoyel, *Solid State Ionics*, 2012, **227**, 119–127.
- 13 F. Croce, G. Appetecchi, L. Persi and B. Scrosati, *Nature*, 1998, **394**, 456–458.
- 14 D. Fenton, J. Parker and P. Wright, Polymer, 1973, 14, 589.
- 15 R. Bouchet, S. Maria, R. Meziane, A. Aboulaich, L. Lienafa, J.-P. Bonnet, T. N. Phan, D. Bertin, D. Gigmes and D. Devaux, *Nat. Mater.*, 2013, 12, 452–457.
- 16 A. M. Stephan, Eur. Polym. J, 2006, 42, 21-42.
- 17 H. Oh, K. Xu, H. D. Yoo, D. S. Kim, C. Chanthad, G. Yang, J. Jin, I. A. Ayhan, S. M. Oh and Q. Wang, *Chem. Mater.*, 2015, 28, 188–196.
- 18 D. R. MacFarlane, N. Tachikawa, M. Forsyth, J. M. Pringle, P. C. Howlett, G. D. Elliott, J. H. Davis, M. Watanabe, P. Simon and C. A. Angell, *Energy Environ. Sci.*, 2014, 7, 232–250.
- 19 M. Armand, F. Endres, D. R. MacFarlane, H. Ohno and B. Scrosati, *Nat. Mater.*, 2009, **8**, 621–629.
- 20 T. Sato, T. Morinaga, S. Marukane, T. Narutomi, T. Igarashi, Y. Kawano, K. Ohno, T. Fukuda and Y. Tsujii, *Adv. Mater.*, 2011, 23, 4868–4872.
- 21 D. Mecerreyes, Prog. Polym. Sci., 2011, 36, 1629-1648.
- 22 J.-H. Choi, Y. Ye, Y. A. Elabd and K. I. Winey, *Macromolecules*, 2013, **46**, 5290–5300.
- 23 P. Zhang, M. Li, B. Yang, Y. Fang, X. Jiang, G. M. Veith, X. G. Sun and S. Dai, *Adv. Mater.*, 2015, 27, 8088–8094.
- 24 N. Matsumi, K. Sugai, M. Miyake and H. Ohno, *Macromolecules*, 2006, 39, 6924–6927.
- 25 Y. Lu, S. K. Das, S. S. Moganty and L. A. Archer, *Adv. Mater.*, 2012, 24, 4430–4435.
- 26 S.-H. Wang, S.-S. Hou, P.-L. Kuo and H. Teng, ACS Appl. Mater. Interfaces, 2013, 5, 8477–8485.
- 27 K. Yin, Z. Zhang, X. Li, L. Yang, K. Tachibana and S.-I. Hirano, *J. Mater. Chem. A*, 2015, 3, 170–178.
- 28 F. Kaneko, S. Wada, M. Nakayama, M. Wakihara, J. Koki and S. Kuroki, *Adv. Funct. Mater.*, 2009, **19**, 918–925.
- 29 J.-C. Daigle, A. Vijh, P. Hovington, C. Gagnon, J. Hamel-Pâquet, S. Verreault, N. Turcotte, D. Clément, A. Guerfi and K. Zaghib, J. Power Sources, 2015, 279, 372–383.
- 30 J. Evans, C. A. Vincent and P. G. Bruce, *Polymer*, 1987, 28, 2324–2328.

- 31 Z. Li, Q. Xia, L. Liu, G. Lei, Q. Xiao, D. Gao and X. Zhou, *Electrochim. Acta*, 2010, **56**, 804–809.
- 32 K. Kimura, H. Matsumoto, J. Hassoun, S. Panero, B. Scrosati and Y. Tominaga, *Electrochim. Acta*, 2015, 175, 134–140.
- 33 C. Zhu, H. Cheng and Y. Yang, J. Electrochem. Soc, 2008, 155, A569–A575.
- 34 G.-T. Kim, S. Jeong, M.-Z. Xue, A. Balducci, M. Winter, S. Passerini, F. Alessandrini and G. Appetecchi, *J. Power Sources*, 2012, 199, 239–246.
- 35 C. Kolbeck, M. Killian, F. Maier, N. Paape, P. Wasserscheid and H.-P. Steinrück, *Langmuir*, 2008, 24, 9500–9507.
- 36 J. L. Nugent, S. S. Moganty and L. A. Archer, *Adv. Mater.*, 2010, 22, 3677–3680.
- 37 P. Agarwal, H. Qi and L. A. Archer, *Nano Lett.*, 2009, **10**, 111–115.
- 38 D. H. Wong, J. L. Thelen, Y. Fu, D. Devaux, A. A. Pandya, V. S. Battaglia, N. P. Balsara and J. M. DeSimone, *Proc. Natl. Acad. Sci. U. S. A.*, 2014, 111, 3327–3331.
- 39 K. H. Choi, S. J. Cho, S. H. Kim, Y. H. Kwon, J. Y. Kim and S. Y. Lee, *Adv. Funct. Mater.*, 2014, **24**, 44–52.
- 40 J. Zhang, J. Zhao, L. Yue, Q. Wang, J. Chai, Z. Liu, X. Zhou, H. Li, Y. Guo and G. Cui, Adv. Energy Mater., 2015, 5, 1501082.
- 41 P. R. Chinnam and S. L. Wunder, *Chem. Mater.*, 2011, 23, 5111–5121.
- 42 N. P. Young, D. Devaux, R. Khurana, G. W. Coates and N. P. Balsara, *Solid State Ionics*, 2014, **263**, 87–94.
- 43 J.-K. Kim, A. Matic, J.-H. Ahn and P. Jacobsson, *J. Power Sources*, 2010, **195**, 7639–7643.
- 44 S. Duluard, J. Grondin, J. L. Bruneel, I. Pianet, A. Grélard, G. Campet, M. H. Delville and J. C. Lassègues, *J. Raman Spectrosc.*, 2008, **39**, 627–632.
- 45 Y. Lu, S. S. Moganty, J. L. Schaefer and L. A. Archer, *J. Mater. Chem.*, 2012, 22, 4066–4072.
- 46 Y. S. Yun, J. H. Kim, S.-Y. Lee, E.-G. Shim and D.-W. Kim, *J. Power Sources*, 2011, **196**, 6750–6755.
- 47 P. Reale, A. Fernicola and B. Scrosati, *J. Power Sources*, 2009, 194, 182–189.
- 48 S. Choudhury, R. Mangal, A. Agrawal and L. A. Archer, *Nat. Commun.*, 2015, **6**, 10101.
- 49 W. Zhou, S. Wang, Y. Li, S. Xin, A. Manthiram and J. B. Goodenough, *J. Am. Chem. Soc.*, 2016, **138**, 9385–9388.
- 50 A. Abouimrane, J. Ding and I. Davidson, *J. Power Sources*, 2009, **189**, 693–696.
- 51 O. Garcia-Calvo, N. Lago, S. Devaraj and M. Armand, *Electrochim. Acta*, 2016, **220**, 587–594.
- 52 L. Porcarelli, A. S. Shaplov, M. Salsamendi, J. R. Nair, Y. S. Vygodskii, D. Mecerreyes and C. Gerbaldi, ACS Appl. Mater. Interfaces, 2016, 8, 10350–10359.
- 53 Q. Pan, D. M. Smith, H. Qi, S. Wang and C. Y. Li, *Adv. Mater.*, 2015, 27, 5995–6001.
- 54 D. Zhang, H. Yan, Z. Zhu, H. Zhang and J. Wang, *J. Power Sources*, 2011, **196**, 10120–10125.
- 55 A. S. Shaplov, D. O. Ponkratov, P. S. Vlasov, E. I. Lozinskaya, L. V. Gumileva, C. Surcin, M. Morcrette, M. Armand, P.-H. Aubert and F. Vidal, *J. Mater. Chem. A*, 2015, 3, 2188– 2198.